Juniper Online
Journal Material Science
ISSN: 2575-856X

Research Article
Volume 10 Issue 2 - February 2026
DOI: 10.19080/JOJMS.2026.10.555785

JOJ Material Sci

Performance of 6061 Deposition Prepared at High Efficiency Based on Hybrid Heat-Source Solid-State Additive Manufacturing

Qian Qiao[a], Dawei Guo[a,b]*, Hongchang Qian[c], Zhong Li[c], Guoshun Yang[d], Chi Tat Kwok[e] and Lap Mou Tam[a,b,e]*

[a]*IDQ Science and Technology (Hengqin, Guangdong), China*

[b]*Institute for the Development and Quality, China*

[c]*National Materials Corrosion and Protection Data Center, Institute for Advanced Materials and Technology, University of Science and Technology Beijing, China*

[d]*Aerospace Engineering Equipment, China*

[e]*Department of Electromechanical Engineering, University of Macau, China*

Submitted: February 09, 2026; **Published:** February 24, 2026

***Corresponding author:** Dawei Guo, IDQ Science and Technology (Hengqin, Guangdong) Co. Ltd., Guangdong, Institute for the Development and Quality, Macao, China

Lap Mou Tama, IDQ Science and Technology (Hengqin, Guangdong) Co. Ltd., Guangdong, Institute for the Development and Quality, Macao, Department of Electromechanical Engineering, University of Macau, Macao, China

Abstract

Additive friction stir deposition, a novel solid-state additive manufacturing technique, may yield insufficient heat, resulting in poor forming quality and compromised mechanical properties of the produced components, when higher production efficiency is required. This study assessed whether hybrid heat-source solid-state additive manufacturing (HHSAM) can improve production efficiency while maintaining component performance. Microstructural characterization, mechanical testing, and electrochemical corrosion analysis were employed to evaluate the performance of Al-6061 depositions fabricated at high efficiency using HHSAM method, achieving a production efficiency of 40kgh. Results demonstrated that the HHSAM deposition exhibited a refined grain structure owing to enhanced thermal evolution and intensified plastic deformation, as evidenced by reduced Fspi and Mspi during in situ monitoring. Microhardness and tensile strength of the HHSAM Al-6061 deposition was enhanced to 107.2HV0.5, 275.5MPa (UTS), 312.5MPa (YS) and 22.1% (EL). Wear resistance of the HHSAM deposition was improved about 2.2 times, owing to grain refinement and precipitation strengthening. Furthermore, the deposition also exhibited superior corrosion resistance, governed by the refined microstructure and the establishment of a more protective passive film.

Keywords: Hybrid heat-source solid-state additive manufacturing (HHSAM); In-situ monitoring; Mechanical performance

Abbreviations: HHSAM: Hybrid Heat-Source Solid-State Additive Manufacturing; AFSD: Additive Friction Stir Deposition; AM: Additive Manufacturing; BD: Build Direction; LD: Longitudinal Direction; RE: Reference; CE: Counter-Electrode; OCP: Open-Circuit Potential; PD: Potentiodynamic Polarization; AGG: Abnormal Grain Growth; IPF: Inverse Pole Figure; PF: Pole Figure; UTS: Ultimate Tensile Strength; YS: Yield Strength

Introduction

Additive friction stirs deposition (AFSD), a novel solid-state additive manufacturing (AM) technique [1,2], was introduced by MELD company to permit repairing, coating, and building fully dense depositions [3-5]. The AFSD method offers clear advantages over powder bed fusion, directed energy deposition, and ultrasonic AM, as it avoids hot cracking, porosity, and the need for secondary densification post processing [6,7]. AFSD has been widely applied for depositing aluminum alloys because of these merits [8,9]. However, fabricating large specimens or alloys with high melting temperatures (e.g., Ni-based and Ti-based alloys) solely via AFSD remains challenging [10,11]. The process does not guarantee a uniform material structure or robust interlayer bonding strength, both governed by thermal evolution during operation. Moreover, frictional heat produced by severe plastic

deformation during layer-by-layer stacking may not maintain the stable temperature range required to ensure adequate material flow and metallic bonding formation [12,13]. Consequently, when higher production efficiency is required, the AFSD method may yield insufficient heat, resulting in poor forming quality and compromised mechanical properties of the produced components. How to improve efficiency while ensuring the mechanical properties of materials remains an unsolved problem.

Our previous work demonstrated the viability of hybrid heat-source solid-state AM (HHSAM), which employs induction heating to deposit uniform Al-6061 components with enhanced performance [14]. Multilayer 5A06 depositions with improved tensile strength and corrosion resistance were also fabricated via HHSAM, which improved the uniformity of plastic deformation flow [15]. Existing research indicates that there are no reports on the deposition efficiency and mechanical properties of aluminum alloys based on HHSAM method. Therefore, this study assessed whether HHSAM can improve production efficiency while maintaining component performance. Production efficiency was set at 40 kgh by adjusting process parameters such as rotation speed and traverse speed to prepare high-quality deposited specimens. A self-developed lightweight tool (in situ process monitoring kit) was employed to record temperature, force, and torque, thus elucidating the structural features of the deposition and evaluating both the deposition and tool-head quality by controlling material flow [16].

In this study, the Al-6061 deposition prepared at high efficiency via HHSAM was monitored in real time for deformation-evolution with varying parameters including temperature (T), upsetting force (F_{ups}), spindle force (F_{spi}), spindle torque (M_{spi}), and bending force (F_{bend}). Simultaneously, the microstructure, mechanical properties, and corrosion resistance of the deposition were analyzed. Depositions fabricated by the conventional AFSD process served as controls to determine the effectiveness of HHSAM. These findings both guide visualization of the solid-state AM process and present a new approach for acquiring high-quality AA6061 depositions.

Experimental Methods

Materials and methods

Table 1: Average chemical compositions of AA6061 alloy.

Element	Al	Mg	Si	Cu	Cr	Zn	Mn	Fe
wt%	Bal.	1.1	0.6	0.4	0.2	<0.2	<0.2	0.7

Figure 1a illustrates the AFSD process for depositing AA6061-T6 feedstock (15mm×15mm×350mm) onto an 8-mm-thick AA6061-T6 substrate. The chemical compositions of the feedstock and substrate are listed in Table 1. Prior to deposition, the feedstock surfaces were spray-coated with a graphite layer to lubricate movement and prevent the rod from being drawn into the deposition tool [17]. In this study, a modified AFSD machine (MSAM-B20X15, Aerospace Engineering Equipment (Suzhou) Co., Ltd., China) fabricated AA6061 depositions comprising 17 layers (each with 3mm thickness). For each layer, the parameters were set: rotation speed (Ω) of 600rpm, a traverse speed (V) of 1000 mm/min, and a feed ratio of 1.2. An *in-situ* process monitoring kit with a 32mm tool diameter and no protrusions [9,10] recorded temperature (T), upsetting force (F_{ups}), spindle force (F_{spi}), spindle torque (M_{spi}), and bending force (F_{bend}) at 1024 Hz with 0.5% accuracy. The hybrid heat was provided by an induction coil (PPC100, Shuangping, China) installed outside the hollow tool Figure 1a. During AFSD deposition, the heat-supply device was deactivated; during HHSAM deposition, induction heating was set at 1.53kW, 16.6 A, and 24.3kHz. Temperature, monitored by the *in-situ* kit, was maintained at approximately 220 °C. A circular-type copper coil with an air-cooling unit converted electrical energy into heat via the magnetic field [18]. As reported previously, a thermocouple was positioned 15mm above the base of the hollow tool, whereas the induction coil was inserted 3mm below the thermocouple. Therefore, the monitored temperature corresponded to the set temperature of the inductor device.

Figure 1b presents images of the obtained AFSD and HHSAM depositions, and Figure 1c illustrates the sampling diagram based on the fabricated deposition. Both depositions exhibited excellent forming quality without visible flaws. The detailed differences in microstructure and properties are discussed below in conjunction with the *in-situ* process monitoring data. Post fabrication, depositions underwent heat treatment in a vacuum annealing furnace (NB380A, Normantherm, China). The heat treatment included solution treatment at 535 °C for 2h, water quenching, aging at 175 °C for 8h, followed by air cooling. The solution treatment ramp rate was 8.5°C/min, with the quenching water temperature at approximately 25°C. Hereafter, specimens are designated as AFSD and HHSAM depositions, respectively.

Microstructure analysis

Specimens for microstructural analysis were machined via wire electrical-discharge machining (Datie Numerical-Control Co., Ltd., Guangdong, China) according to the sampling diagram Figure 1c. Specimens extracted from the deposition center were ground with 400-grit SiC paper, then sequentially polished with

How to cite this article: Qian Q, Dawei G, Hongchang Q, Zhong L, Guoshun Y. Performance of 6061 Deposition Prepared at High Efficiency Based on Hybrid Heat-Source Solid-State Additive Manufacturing. JOJ Material Sci. 2025; 10(2): 555785. DOI: 10.19080/JOJMS.2026.10.555785

9,3, and 1μm polycrystalline diamond suspensions, and finally vibrationally polished with 0.02μm colloidal silica (VibroMet 2, Buehler) to minimize surface roughness and achieve a mirror-like finish. The cross-sectional microstructure was examined using an optical microscope (Olympus GX71). Electron back-scattered diffraction (EBSD, Symmetry S2, Oxford, UK) was performed to analyze grain size, obtaining a large-area EBSD map (3 mm×3 mm). EBSD data were post-processed using Aztec-Crystal 2.1 software in accordance with ASTM Standard 2627-13 [19].

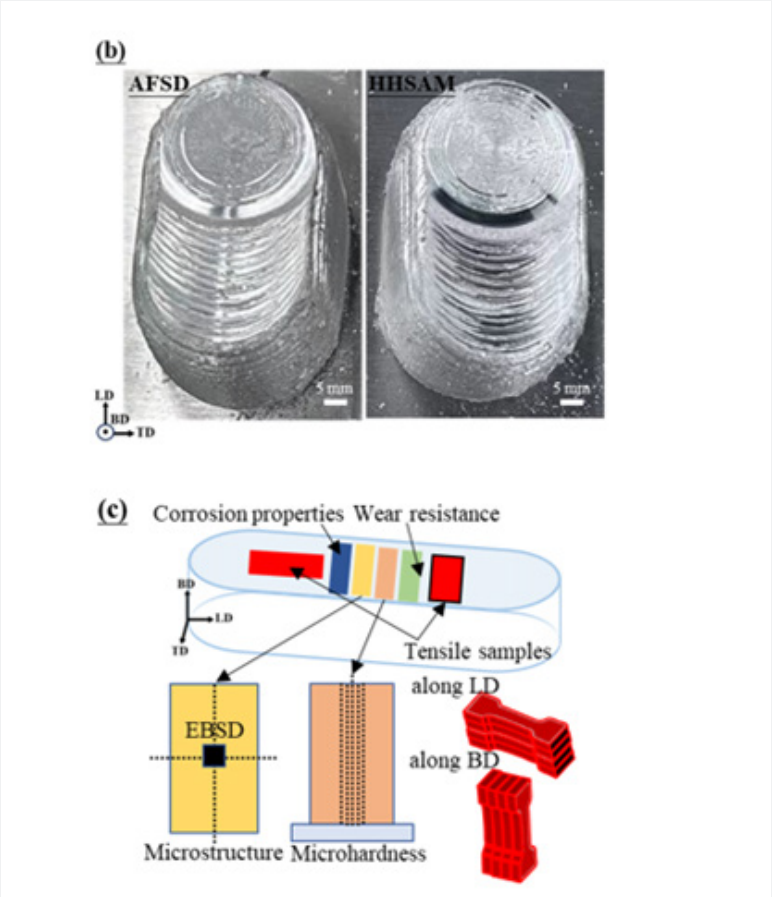

Figure 1: (a) Schematic of the AFSD process. (b) Physical images of the fabricated depositions. (c) Sampling diagram.

Mechanical performance

Specimens sectioned parallel to the build direction (BD) and transverse plane were used for microhardness measurements. Microhardness was evaluated with a Vickers microhardness tester (Qpix Control2, Qness, Germany) on cross-sections using a 100g load, 15s dwell time, and 0.5mm step size Figure 1c.

Tensile tests were conducted at room temperature along the longitudinal direction (LD) and BD of the depositions following ASTM standard methods with an 8mm gauge length [20]. Tensile experiments employed a computer-controlled testing machine (WDW-20, Shanghai Bairoe Test Instrument Co., Ltd., China) at a strain rate of 2mm/min under quasistatic conditions, with triplicate measurements ensuring statistical accuracy.

Wear tests were performed using a ball-on-plate tribometer (UMT-2, Bruker, USA) [21]. A 440C steel ball (6mm diameter) served as the counter-surface and slid against the specimen in reciprocating mode under a 2 N load at 10 Hz for 1 h at room temperature. Worn surface morphologies were evaluated with a three-dimensional (3D) optical microscope (Contour GT-X3, Bruker, Germany) using Vision 64 software to measure wear volume. Surface profiles across the wear track were measured, and the wear track volume was estimated by multiplying the area below zero (relative to the unworn region) by the track length [22]. All tests were repeated in triplicate to ensure reproducibility.

Electrochemical properties

Corrosion tests were conducted using a potentiostat (Versastat-3F, Princeton, USA) in 3.5wt% NaCl solution. A saturated calomel electrode (SCE, +0.244V vs. SHE at 2°C) and a

How to cite this article: Qian Q, Dawei G, Hongchang Q, Zhong L, Guoshun Y. Performance of 6061 Deposition Prepared at High Efficiency Based on Hybrid Heat-Source Solid-State Additive Manufacturing. JOJ Material Sci. 2025; 10(2): 555785. DOI: 10.19080/JOJMS.2026.10.555785

pair of graphite rods were used as the reference (RE) and counter-electrode (CE), respectively. After a 1h open-circuit potential (OCP) measurement resulting in a stable potential. Electrochemical impedance spectroscopy tests were conducted at OCP with a 10^{-} mV voltage perturbation over a frequency range from 10mHz to 100kHz. Subsequently, potentiodynamic polarization (PD) tests were initiated from 0.25 VSCE below OCP at a scanning rate of 1mV/s. To ensure reliability, at least three replicates of each specimen were tested Figure 2. General corrosion results were analyzed using Nyquist and Bode plots fitted with ZSimp Win software. Corrosion potential (E_{corr}) and corrosion current density (I_{corr}) were extracted from the PD curves via Tafel extrapolation using Power C_{orr} V.2.42.

Results and Discussion

Monitoring results

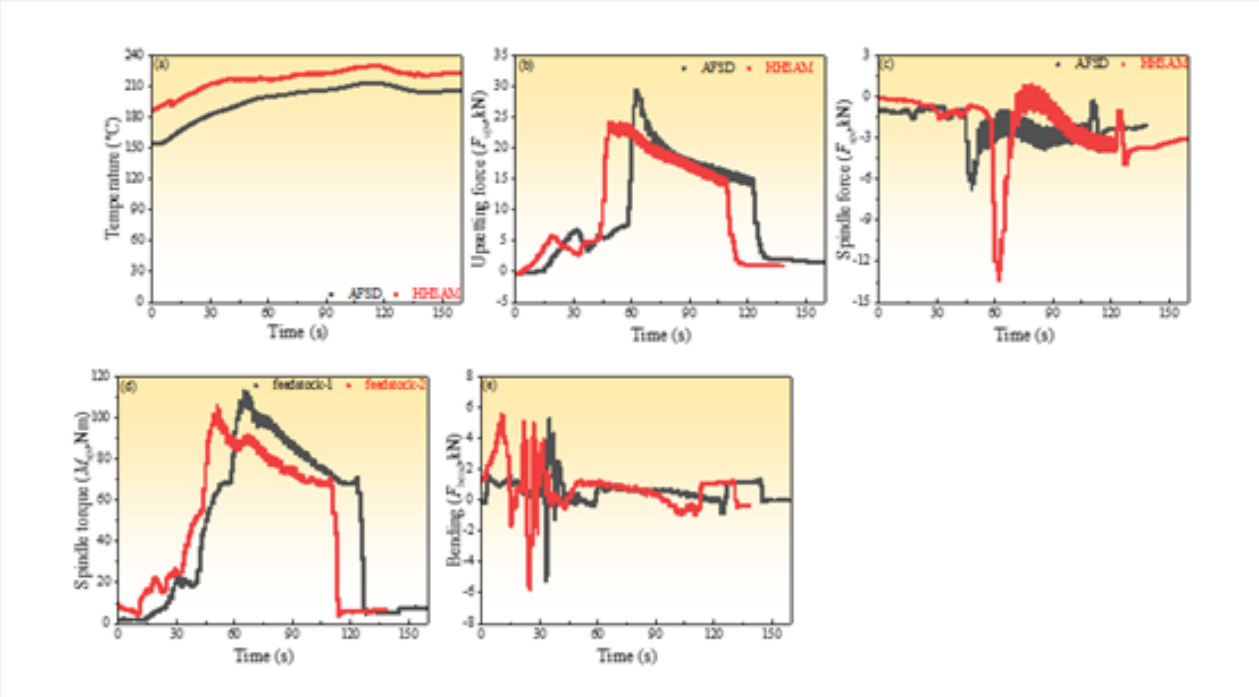

Figure 2: The monitored real-time results of the AFSD and HHSAM depositions: (a) T, (b) Fups, (c) Fspi, (d) Mspi and (e) Fbend.

Figure 3 illustrates real-time temperature, force, and torque evolution collected by the monitoring kit during the manufacturing process. The layer-by-layer deposition produced multiple peaks, each corresponding to a single layer. The data revealed that temperature, force, and torque increased gradually to a maximum before dropping owing to tool retraction at the onset of the next layer deposition. Depositing a new top layer re-initiated heating and compressing cycles over the underlying layers, with cycle amplitude decreasing as the high-temperature tool head moved away from the deposited interface. For analytical convenience, the average values of the real-time data are summarized in Table 2. Notably, the HHSAM process yielded an average temperature of approximately 228.4 °C, compared to 205.7 °C for the AFSD process, indicating that hybrid heat effectively supplied additional energy during fabrication. Figure 3b indicates that Fups for the HHSAM deposition was approximately 17.49kN, likely associated with the heating process. The elevated temperature induced greater thermal expansion at the tip of the Al-6061 feedstock, with the expansion constrained by the hollow tool outlet, generating a reaction force that promoted feedstock movement. Consequently, a larger Fups was required to advance the feedstock relative to that observed in the AFSD deposition (-2.29kN).

From Figure 3c presents Fspi, the resultant force along BD. It comprises the positive friction force ("+BD") from the advancing feedstock and the negative drag force exerted by the softened material on the spindle ("−BD"). When the hollow tool pressed firmly against the deposited layer, the interface restricted plastic deformation, compressing it to a fixed thickness and inducing an upward reaction force that imposed positive pressure on

How to cite this article: Qian Q, Dawei G, Hongchang Q, Zhong L, Guoshun Y. Performance of 6061 Deposition Prepared at High Efficiency Based on Hybrid Heat-Source Solid-State Additive Manufacturing. JOJ Material Sci. 2025; 10(2): 555785. DOI: 10.19080/JOJMS.2026.10.555785

the spindle. At the feedstock tip, plastic deformation generated a substantial static friction force against the inner wall of the hollow tool head as the material expanded and deformed. As the feedstock moved downward, the hollow tool experienced a downward drag force while the spindle encountered a negative tensile force. These combined factors influenced the evolution of F_{spi}. For AFSD specimens, the heat was insufficient to soften the feedstock fully, resulting in limited plastic deformation and a lower F_{spi} (−6.71kN). By contrast, during HHSAM deposition the feedstock tip experienced elevated temperatures, increasing its susceptibility to plastic deformation and enhancing its flow. Consequently, the negative drag force predominated, yielding an F_{spi} of −12.12kN for the HHSAM specimen Table 2. Moreover, the HHSAM deposition exhibits a lower Mspi (81.11Nm) and higher Fbend (0.78kN) than the AFSD deposition (87.49Nm and 0.49kN). Induction heating thoroughly softens the feedstock and enhances material flow. Simultaneously, it reduces the viscosity and strain rate of the material, which ultimately decreases M_{spi} Table 2 [23]. The improved flow behavior of the HHSAM specimen increases F_{bend}.

Table 2: Average monitored results of AFSD and HHSAM depositions.

Specimen	T, °C	F_{ups}, kN	F_{spi}, kN	M_{spi}, Nm	F_{bend}, kN
AFSD	205.7	17.49	−12.12	87.49	0.49
HHSAM	228.4	−2.29	−6.71	81.11	0.78

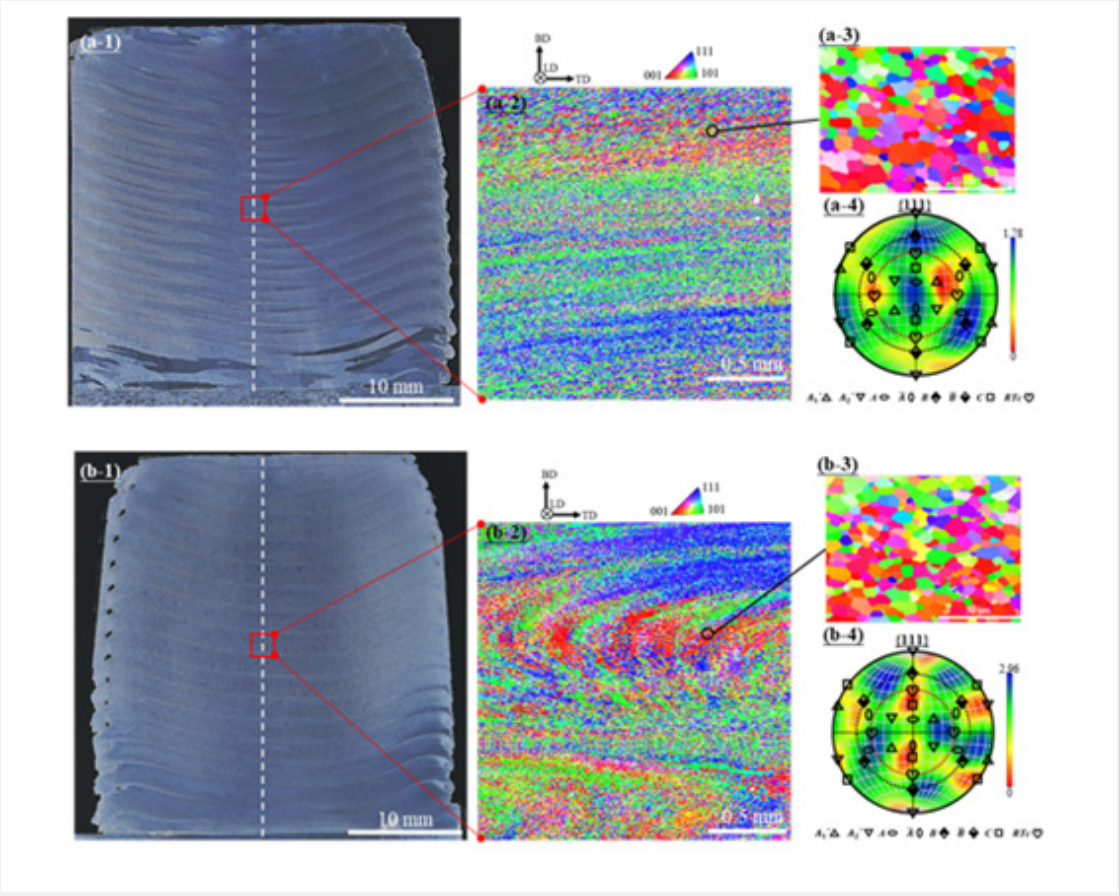

Figure 3: (1) Macrostructure, (2) large-area inverse pole figure (IPFs), (3) high magnified (1000x) IPFs and (4) pole figure (PF) results of AFSD and HHSAM deposition.

Microstructure observation

Figure 3-1 presents the optical morphology of the AFSD and HHSAM deposition along BD, revealing a distinct layer-by-layer structure. The absence of defects such as cracks and pores originates from the robust plastic deformation process. Significantly, abnormal grain growth (AGG) is detected at the bottom and top layers of the AFSD deposition. The AGG phenomenon was induced by unstable heat evolution; the

How to cite this article: Qian Q, Dawei G, Hongchang Q, Zhong L, Guoshun Y. Performance of 6061 Deposition Prepared at High Efficiency Based on Hybrid Heat-Source Solid-State Additive Manufacturing. JOJ Material Sci. 2025; 10(2): 555785. DOI: 10.19080/JOJMS.2026.10.555785

temperature gradient caused microstructural inhomogeneity and significant variations in residual stress, resulting in grain size differences. By contrast, the HHSAM deposition exhibited a refined microstructure with uniform grain size, indicating a balanced thermodynamic driving force. This uniformity promoted even stress distribution and effectively curtailed AGG. Additionally, our previous work [9] demonstrated that Al (Fe, Mn) Si particles formed within the HHSAM-HT 6061 specimen, and their pinning effect further mitigated AGG.

Figure 3 depicts the EBSD results, including inverse pole figure (IPF) and pole figure (PF) images of the depositions, facilitating a detailed comparison of their structural differences. The large-area and 1000× IPF images illustrate refined equiaxed grains resulting from dynamic recrystallization. Compared with the AFSD deposition Figure 3a, the HHSAM deposition Figure 3b exhibits a distinct fish-scale pattern, indicating an enhanced layer-wise material flow. The induction hybrid heat source provides sufficient heat to soften the material, thereby improving the stirring efficiency of the hollow tool and promoting material flow. This process contributes to grain refinement. Based on the large-area EBSD results, the average grain sizes of the AFSD and HHSAM depositions were calculated as 8.9±1.2μm and 5.6±0.8μm, respectively. The additional thermal exposure induced dynamic recrystallization in the parent grains, resulting in finer grains [24]. A 2 μm step size was employed for the large-area EBSD observation, which is lower than the average grain size, thereby rendering the grain size data significant. The deviation from the standard FCC texture is depicted in Figure 3a and Figure 3b. The results revealed that the primary texture component in AFSD deposition was A, with a maximum texture density of 1.78. For HHSAM deposition, the B and C components dominated, contributing to the denser deformation. The monitored data accounted for the higher strain observed during the HHSAM process. Table 2 indicates that HHSAM deposition exhibited higher Fbend and lower M_{spi}, suggesting that increased material flow induced greater plastic strain.

Mechanical properties

Figure 4 presents the microhardness and tensile results, illustrating the mechanical behavior of AFSD and HHSAM depositions. Notably, compared to the AFSD specimen (79.8±.7 HV0.5), the HHSAM deposition achieved a higher microhardness (107.2±3.0 HV0.5; Table 3). Moreover, microhardness mapping of HHSAM deposition was more uniform, indicating a stable microstructure under homogeneous thermal conditions. Concurrently, additional heat during HHSAM promoted precipitate dissolution and increased solute atom concentration. Consequently, a supersaturated solid solution with a high vacancy density formed following heat treatment, augmenting the microhardness of the deposition [25]. Figure 4b details the ultimate tensile strength (UTS), yield strength (YS), and elongation, as listed in Table 3. For the test specimen along LD, the AFSD samples exhibited UTS, YS, and elongation of 259.03±7.69 MPa, 298.45±3.24 MPa, and 17.5±1.92%, respectively. Concurrently, the corresponding HHSAM values increased to 275.45±7.69 MPa, 312.53±3.24 MPa, and 22.13±1.92%.

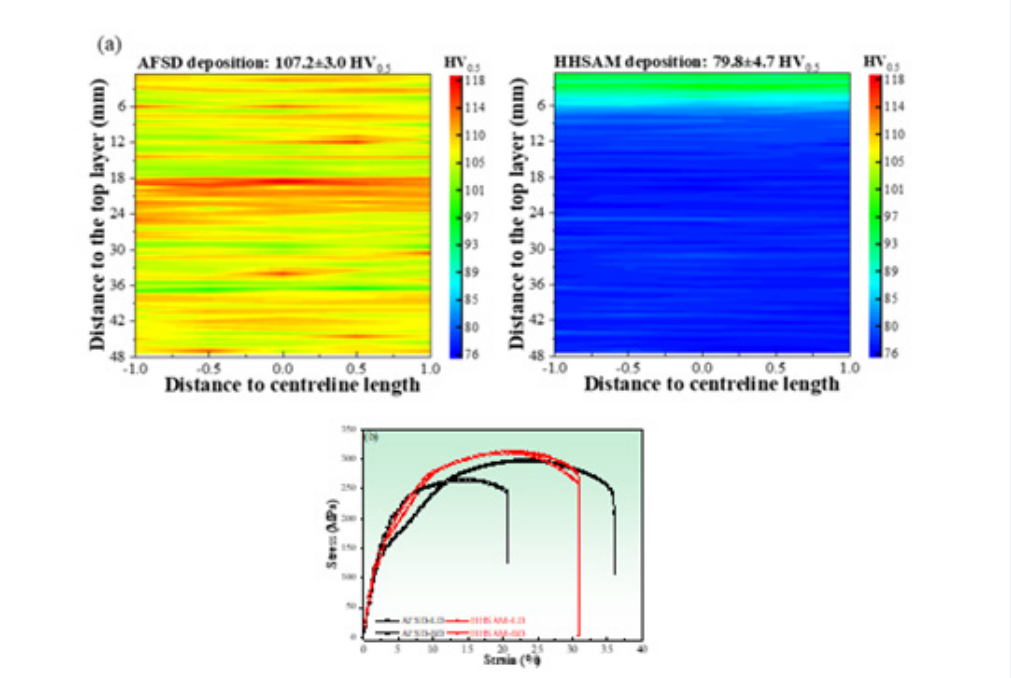

Figure 4: (a) Micro-hardness and (b) stress-stain plots of the fabricated depositions.

How to cite this article: Qian Q, Dawei G, Hongchang Q, Zhong L, Guoshun Y. Performance of 6061 Deposition Prepared at High Efficiency Based on Hybrid Heat-Source Solid-State Additive Manufacturing. JOJ Material Sci. 2025; 10(2): 555785. DOI: 10.19080/JOJMS.2026.10.555785

Table 3: Mechanical properties of feedstock and AA6061 depositions under different *D*.

	AFSD Deposition	HHSAM Deposition
Microhardness (HV0.5)	79.8±4.7	107.2±3.0
UTS-LD (MPa)	259.03±7.69	275.45±7.69
YS-LD (MPa)	298.45±3.24	312.53±3.24
EL-LD (%)	17.5±1.92	22.13±1.92
UTS-BD (MPa)	223.43±12.53	271.84±16.27
YS-BD (MPa)	264.87±19.06	310.97±0.58
EL-BD (%)	12.5±3.1	19.88±2.32

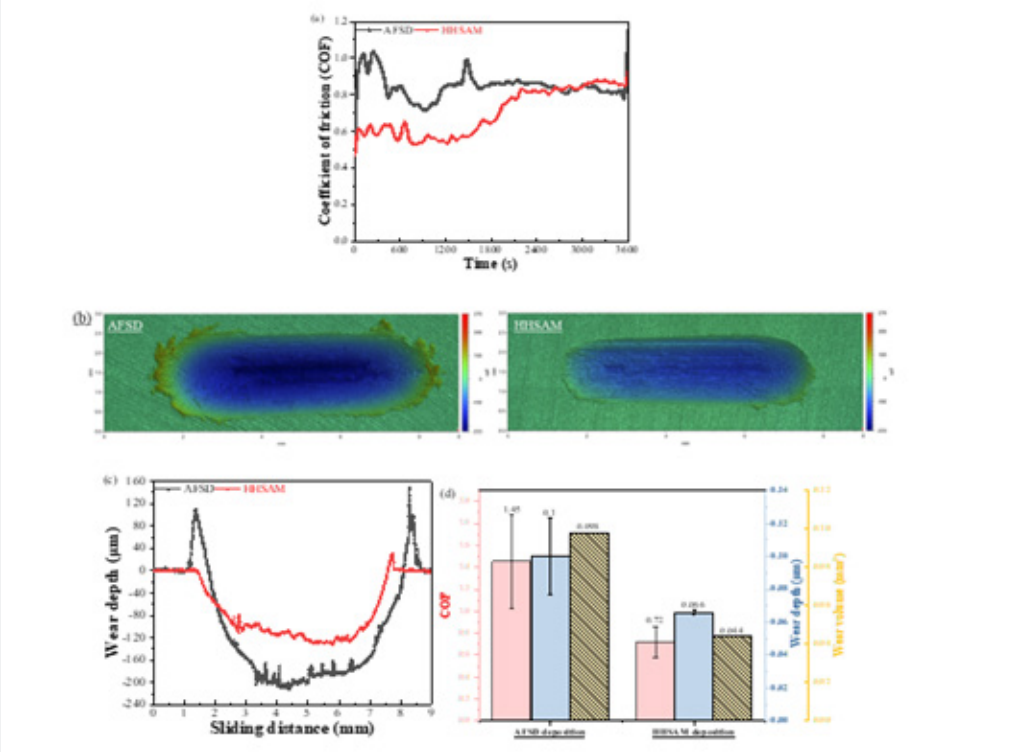

Figure 5: (a) COF, (b) 2D images, (c) wear depth of the AFSD and HHSAM depositions. (d) organizes the wear results of the depositions.

Similarly, the tensile properties along the BD also improved substantially. The UTS, YS, and EL of the HHSAM samples reached 271.84±16.27 MPa, 310.97±0.58 MPa, and 19.88±2.32 %, respectively, compared with the AFSD deposition, which produced 223.43±12.53 MPa, 264.87±19.06 MPa, and 12.5±3.1%. This enhancement primarily resulted from grain refinement. AA6061 is a precipitate-hardening alloy, and the induced precipitates positively affect mechanical properties [26]. Thus, the deposition enhancement may also stem from precipitate strengthening. Consistent with the research of [27] the induced Mg_2Si and β″ phases significantly increased hardness by effectively restraining dislocation movement [27]. As noted in the discussion and our previous research [9], Al (Fe, Mn) Si was present in the HHSAM deposition, acting as obstacles to dislocations and yielding higher tensile strength. Notably, the EL enhancement in the HHSAM deposition indicates improved ductility and bonding strength, primarily attributed to grain refinement, which accommodated additional dislocations and enhanced the capacity of the material for plastic deformation evolution [28]. These results confirm that HHSAM effectively enhances softened material fluidity during fabrication, increases bonding strength between deposited layers, and thus improves structural density, uniformity, and mechanical properties of deposited components along BD.

Figure 5a presents the COF evolution for each specimen during wear testing. In these tests, the deposition surface contacts the 440C counter face, and interlocking asperities at the junction elevate friction. This raises the force required to overcome static friction, causing a sudden COF increase during the static-to-

How to cite this article: Qian Q, Dawei G, Hongchang Q, Zhong L, Guoshun Y. Performance of 6061 Deposition Prepared at High Efficiency Based on Hybrid Heat-Source Solid-State Additive Manufacturing. JOJ Material Sci. 2025; 10(2): 555785. DOI: 10.19080/JOJMS.2026.10.555785

kinetic friction transition, after which COF stabilizes near 1800s for all specimens. The HHSAM deposition exhibits a stable COF of 0.72±0.14 compared to 1.45±0.42 for AFSD deposition. 3D optical profilometry of the worn regions Figure 6 reveals maximum wear depths of 0.100±0.023μm and 0.066±0.001μm for AFSD and HHSAM, respectively. Moreover, the HHSAM worn surface displays a slight groove, indicating that its structural density limits plastic deformation during wear and reduces abrasive wear. Conversely, the AFSD worn scar exhibits severe plastic deformation with plowing marks parallel to the sliding direction. As listed in Table 3, HHSAM deposition demonstrates superior mechanical properties that enhance wear resistance. The homogeneous microstructure and increased tensile strength restricted plastic strain and extended service life before reaching the critical strain threshold for fracture [29]. The wear volume of the specimens, depicted in Figure 6, indicated that the HHSAM deposition exhibited a lower volume (0.044±0.001mm^3), 0.33 times that of the AFSD deposition (0.066±0.001 mm^3). This finding demonstrates that HHSAM provided superior wear resistance by inhibiting crack nucleation and surface-parallel propagation, thereby mitigating delamination [30]. Additional heating improved flow, mixing, and distribution of the deposits during HHSAM, resulting in enhanced structural density and wear resistance.

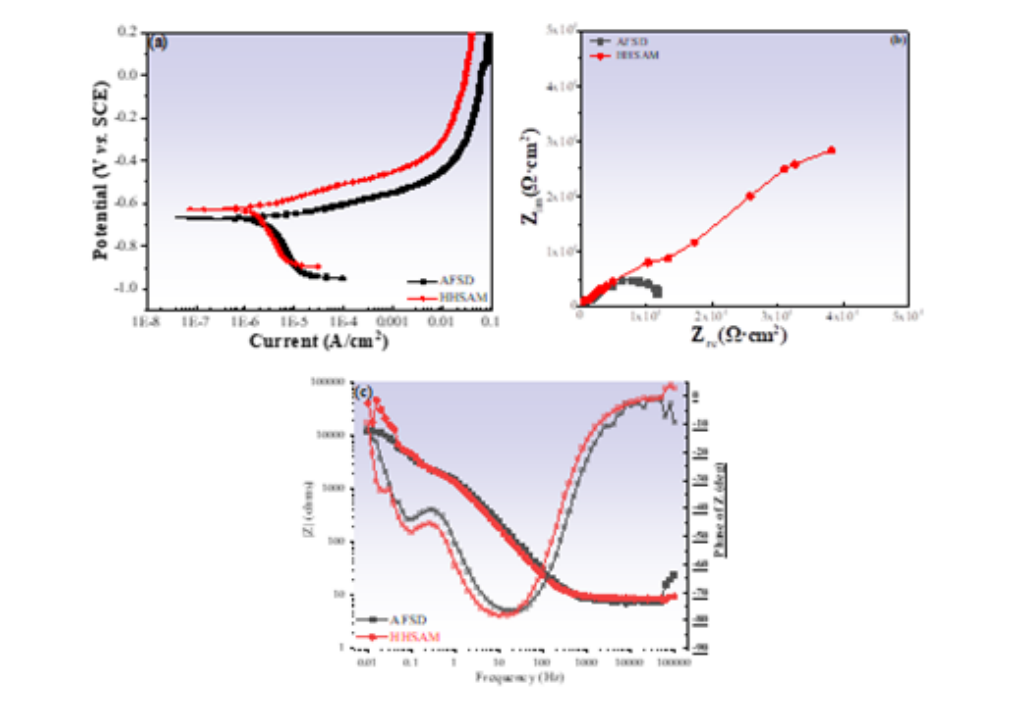

Figure 6: (a) PD curves, (b) Nyquist plots, and (c) Bode plots for the specimens.

Corrosion resistance

Figure 6a presents the corrosion behavior of AFSD and HHSAM depositions immersed in a 3.5wt% NaCl solution, with corresponding electrochemical parameters (corrosion potential (E_{corr}) and corrosion current density (I_{corr})) listed in Table 3. The slightly more negative Ecorr of the AFSD deposition (−673.2±31.20 mV), compared to HHSAM (−624.16±27.15mV), suggests that Sc addition increased the tendency for corrosion initiation; however, it did not govern corrosion kinetics. HHSAM exhibited a significantly lower Icorr (1.78±0.45μA/cm^2) than AFSD (2.84±0.45μA/cm^2), indicating enhanced corrosion resistance. The manufacturing process plays a crucial role in refining deposition microstructure, with Icorr decreasing proportionally as grain size reduces [31]. The refined grain structure of the HHSAM deposition enhanced formation of a more protective oxide layer and resulted in a lower I_{corr} [32]. Precipitates within the deposition acted as barriers against chloride ion diffusion, further slowing the corrosion process [33]. The Nyquist and Bode plots in Figure 6 were analyzed with an equivalent circuit, and fitted results are summarized in Table 4, where Rs denotes the solution resistance, R_1 and Q_1 represent the resistance and capacitance of the induced passive film, respectively, R_2 indicates the charge transfer resistance, and Q_2 denotes the double layer capacitance. Notably, the Nyquist plot in Figure 6 revealed that the HHSAM deposition exhibited a larger capacitive arc diameter than the AFSD specimen, indicating improved protection against corrosive media degradation. This finding aligns with the PD result and was further corroborated by R_1. The Rf value of the HHSAM deposition (2.48±0.70 ×105Ω·cm^2) exceeded that of the AFSD specimen

How to cite this article: Qian Q, Dawei G, Hongchang Q, Zhong L, Guoshun Y. Performance of 6061 Deposition Prepared at High Efficiency Based on Hybrid Heat-Source Solid-State Additive Manufacturing. JOJ Material Sci. 2025; 10(2): 555785. DOI: 10.19080/JOJMS.2026.10.555785

(2.31±1.45×105 Ω·cm²), confirming that the induced passive film on the HHSAM deposition provided enhanced resistance and corrosion protection, thus reducing the overall corrosion rate. The observed improvement is attributed to the formation of a more stable and compact oxide layer, rendering the material less susceptible to corrosion. The HHSAM deposition exhibited a slightly higher R_2 value (68.62±4.92 × 105 Ω·cm²), indicating enhanced corrosion resistance [34]. The micro-galvanic effect induced by particles did not influence the HHSAM deposition; rather, the improved corrosion resistance relative to the AFSD specimen was primarily attributable to the refined microstructure and formation of a more protective passive film.

Table 4: Corrosion parameters of the specimens.

	AFSD Specimen	HHSAM Specimen
E_{corr} (mV)	−673.2 ± 31.20	−624.16 ± 27.15
I_{corr} (μA/cm²)	2.84 ± 0.45	1.78 ± 0.45
R_s (Ω·cm²)	4.46 ± 1.10	9.27 ± 1.24
R_1 (105Ω·cm²)	2.31 ± 1.45	2.48 ± 0.70
Q_1 (10-5 F/cm²)	12.58 ± 2.13	35.72 ± 1.17
n_1	0.88 ± 0.15	0.98 ± 0.10
R_2 (105 Ω·cm²)	22.82 ± 5.51	68.62 ± 4.92
Q_2 (10-5 F/cm²)	2.33 ± 0.91	15.40 ± 1.15
n_2	0.61 ± 0.08	0.74 ± 0.11
λ_2	0.47 ± 0.04	0.46 ± 0.06

Conclusion

This study employed microstructural characterization, mechanical, and electrochemical corrosion testing to investigate the performance of the Al6061 deposition fabricated via the efficient HHSAM method. The production efficiency reached 40 kgh. Results indicate that the HHSAM deposit exhibits a refined grain structure owing to sufficient thermal evolution and stronger plastic deformation, as confirmed by in situ measurements (i.e., reduced Fspi and Mspi). Additionally, the microhardness and tensile strength of the HHSAM Al-6061 deposition was enhanced to 107.2HV0.5, 275.5MPa (UTS), 312.5 MPa (YS) and 22.1% (EL). Wear resistance of the HHSAM 6061 deposition was improved about 2.2 times, owing to grain refinement and precipitation strengthening. Furthermore, its enhanced corrosion resistance compared to the AFSD specimen is primarily attributable to the refined microstructure and formation of a more protective passive film.

Funding

The authors sincerely acknowledge the financial support received from the Science and Technology Development Fund (FDCT) of Macau SAR (0110/2023/AMJ), and the National Key Research and Development Program of China (2023YFE0205300).

Conflicts of Interest

The authors declare that they have no known competing financial interests or personal relationships that could have appeared to influence the work reported in this paper.

Author Contributions

Qian Qiao: Formal analysis, Investigation, Writing-Original Draft, Writing-Review and Editing, Dawei Guo: Supervision, Hongchang Qian, Zhong Li and Guoshun Yang: Visualization, Chi Tat Kwok: Visualization, Lap Mou Tam: Funding acquisition.

Acknowledgement

The authors sincerely acknowledge the financial support received from the Science and Technology Development Fund (FDCT) of Macau SAR (0110/2023/AMJ) and the National Key Research and Development Program of China (2023YFE0205300).

References

1. Olhan S, Antil B, Behera BK (2025) Progress in metal additive manufacturing using innovative solid-state friction stir-based techniques. J Alloys Compd 1010: 177395.
2. Olhan S, Antil B, Behera BK (2025) Synergistic effect of different high-performance fibers on the microstructural evolution and mechanical performance of novel hybrid metal matrix composites produced via friction stir processing for automotive applications. P Mech Eng Bj Eng 239(1-2): 236-249.
3. ASTM ISO/ASTM52900-21 (2021) Additive Manufacturing-General Principles-Fundamentals and Vocabulary. ASTM: West Conshohocken, PA, USA.
4. Yu HZ, Jones ME, Brady GW, Griffiths RJ, Garcia D, et al. (2018) Hardwick, Non-beam-based metal additive manufacturing enabled by additive friction stir deposition. Scr Mater 153: 122-130.
5. Rivera OG, Allison PG, Jordon JB, Rodriguez OL, Brewer LN, (2017) Microstructures and mechanical behavior of Inconel 625 fabricated by solid-state additive manufacturing. Mate Sci Eng A 694: 1-9.

How to cite this article: Qian Q, Dawei G, Hongchang Q, Zhong L, Guoshun Y. Performance of 6061 Deposition Prepared at High Efficiency Based on Hybrid Heat-Source Solid-State Additive Manufacturing. JOJ Material Sci. 2025; 10(2): 555785. DOI: 10.19080/JOJMS.2026.10.555785

6. Phillips BJ, Avery DZ, Liu T, Rodriguez OL, Mason CJT, et al. (2019) Microstructure-deformation relationship of additive friction stir-deposition Al-Mg-Si. Mater 7: 100387.

7. Khodabakhshi F, Gerlich AP (2018) Potentials and strategies of solid-state additive friction-stir manufacturing technology: A critical review. J Manuf Process 36: 77-92.

8. Griffiths R, Perry M, Sietins J, Zhu Y, Hardwick N, et al. (2018) A perspective on solid-state additive manufacturing of aluminum matrix composites using MELD. J Mater Eng Perform 28: 648-656.

9. Avery DZ, Rivera OG, Mason CJT, Phillips BJ, Jordon JB, et al. (2018) Fatigue behavior of solid-state additive manufactured Inconel 625. JOM 70: 2475-2484.

10. Gopan V., Wins KLD, Surendran A (2021) Innovative potential of additive friction stir deposition among current laser-based metal additive manufacturing processes: A review. CIRP J Manuf Sci Technol 32: 228-248.

11. Olhan S, Antil B, Maimí P, Behera BK (2025) Advances in 4D printing of polymeric composite smart materials. Compos Struct 377: 119859.

12. Olhan S, Khatkar V, Behera BK (2023) Novel high-performance textile fiber-reinforced aluminum matrix structural composites fabricated by FSP. MSEB 289: 116265.

13. Olhan S, Khatkar V, Behera BK (2022) Impact behavior of long glass fiber reinforced aluminum metal matrix composite prepared by friction stir processing technique for automotive. Compos Mater 56(14): 2157-2167.

14. Qiao Q, Tam CW, Lam WI, Wang K, Guo D, et al. (2025) Hybrid heat-source solid-state additive manufacturing: A method to fabricate high performance AA6061 deposition. Journal of Materials Science & Technology 228: 107-124.

15. Qiao Q, Chen X, Lam WI, Lin Y, Wang H, et al. (2025) Hybrid heat-source solid-state additive manufacturing of 5A06 deposition with favorable mechanical and electrochemical performance. NPJ Materials Degradation.

16. Garcia D (2021) Investigation of the Processing History during Additive Friction Stir Deposition using In-process Monitoring Techniques, Doctor of Philosophy in Materials Science and Engineering.

17. Phillips BJ, Williamson CJ, Kinser RP, Jordon JB, Doherty KJ, et al. (2021) Microstructural and mechanical characterization of additive friction stir-deposition of aluminum alloy 5083 effect of lubrication on material anisotropy. Materials 14(21): 6732.

18. Prakaash VGV, Vignesh A, Lakshminarayanan AK, Balasubramanian V (2015) Role of Induction preheating on tool wear and properties of friction stir welded 409M stainless steel joints. Appl Mech Mater 787: 401-405.

19. ASTM (2014) Standard Practice for Determining Average Grain Size Using Electron Backscatter Diffraction (EBSD) in Fully Recrystallized Polycrystalline Materials. ASTM International: West Conshohocken, PA, USA.

20. ASTM (2017) Standard Test Method for Strain-Controlled Fatigue Testing. ASTM, International: West Conshohocken, PA, USA.

21. ASTM G119-09 (2021) Standard Guide for Determining Synergism Between Wear and Corrosion. ASTM International: West Conshohocken, PA, USA.

22. Pina VG, Amigó V, Muñoz AI (2016) Microstructural, electrochemical and tribo-electrochemical characterization of titanium-copper biomedical alloys Corros Sci 109: 115-125.

23. Sun YF, Shen JM, Morisada Y, Fujii H (2014) Spot friction stirs welding of low carbon steel plates preheated by high frequency induction. Mater Des 54: 450-457.

24. Li H, Lin J, Dean TA, Wen SW, Bannister AC (2009) Modelling mechanical property recovery of a line pipe steel in annealing process. Int J Plast 25(6): 1049-1065.

25. Li D, Yang X, Cui L, He F, Shen H (2014) Effect of welding parameters on microstructure and mechanical properties of AA6061-T6 butt welded joints by stationary shoulder friction stir welding. Materials & Design 64: 251-260.

26. Misumi K, Kaneko K, Nishiyama T, Maeda T, Yamada K, et al. (2014) Three-dimensional characterization of interaction between β″ precipitate and dislocation in Al-Mg-Si alloy. J Alloys Compd 600: 29-33.

27. Rao PN, Singh D, Brokmeier HG, Jagannathan R (2015) Effect of ageing on tensile behavior of ultrafine grained Al 6061 alloy. Mater Sci Eng A 641: 391-401.

28. Zavari S, Bagheri E, Ding H, Adibi N, Eller M, et al. (2025) The influence of additive friction stirs deposition process on mechanical properties, corrosion resistance, and electrical conductivity of Al5086-H32 alloy. Progress in Additive Manufacturing 10: 7791-7802.

29. Tanwar RS, Jhavar S (2025) Microstructure and tribological characterization of thin wall of bimetallic austenitic steel fabricated through wire arc additive manufacturing (WAAM). Applications in Engineering Science 23: 100241.

30. Wang L, Okugawa M, Liu Y, Cho K, Yasuda HY, et al. (2025) NiTi coating formation on Ti for enhanced wear resistance utilizing electron-beam additive manufacturing technique. Surfaces and Interfaces 72: 107024.

31. Deng Y, Yin Z, Zhao K, Duan J, Hu J, et al. (2012) Effects of Sc and Zr microalloying additions and aging time at 120 C on the corrosion behavior of an Al–Zn–Mg alloy. Corrosion Science 65: 288-298.

32. Ralston KD, Fabijanic D, Birbilis N (2011) Effect of grain size on corrosion of high purity aluminum. Electrochimica Acta 56(4): 1729-1736.

33. Sareekumtorn P, Chaideesungnoen S, Muangjunburee P, Oo HZ (2024) The electrochemical corrosion performance of aluminum alloys grade 6082-T6 weld repair. Materials Research Express 11(8): 086512.

34. Shen C, Zhang J, Ge J (2011) Microstructures and electrochemical behaviors of the friction stir welding dissimilar weld. Journal of Environmental Sciences 23: S32-S35.

How to cite this article: Qian Q, Dawei G, Hongchang Q, Zhong L, Guoshun Y. Performance of 6061 Deposition Prepared at High Efficiency Based on Hybrid Heat-Source Solid-State Additive Manufacturing. JOJ Material Sci. 2025; 10(2): 555785. DOI: 10.19080/JOJMS.2026.10.555785

DOI: 10.19080/JOJMS.2026.10.555785

How to cite this article: Qian Q, Dawei G, Hongchang Q, Zhong L, Guoshun Y. Performance of 6061 Deposition Prepared at High Efficiency Based on Hybrid Heat-Source Solid-State Additive Manufacturing. JOJ Material Sci. 2025; 10(2): 555785. DOI: 10.19080/JOJMS.2026.10.555785